SCANNING Vol. 19, 416–425 (1997)
© FAMS, Inc.

Received October 20, 1996
Accepted with revision December 20, 1996

Scanning Electron Microscopy Imaging of Microcracks and Charging Phenomena on a Laser-Damaged CaF_2 Surface

H. JOHANSEN, W. ERFURTH, S. GOGOLL,* E. STENZEL,* M. REICHLING,* E. MATTHIAS*

Max-Planck-Institut für Mikrostrukturphysik, Halle; * Freie Universität Berlin, Fachbereich Physik, Berlin, Germany

Summary: Systematic scanning electron microscopy (SEM) investigations of charging phenomena on a laser-damaged CaF_2 surface have been carried out as a function of primary electron energy. To this purpose, we imaged an uncoated trapezoidal area of about 400 μm^2 surrounded by a carbon-covered surface at ground potential. It was located at the periphery of a laser-fractured spot and contained microcracks that served to define the local contrast. Areal surface charging was inspected by comparing the brightness of the uncovered area with that of its surrounding. Microcracks were imaged using backscattered (BSE) and secondary (SE) electrons, and optimal imaging conditions were established for both techniques. The best contrast of the fracture pattern was obtained with 20 keV primary electrons in BSE composition mode. In SE mode, the microstructure was more or less blurred, except for 5 keV and 25° surface inclination where the cracks showed an enhanced SE emission, which might originate from occupied defect states in the band gap.

Key words: scanning electron microscopy imaging of CaF_2, charging phenomena, lateral size effect, laser-induced microcracks

Introduction

Scanning electron microscopy (SEM) is a key technique for analyzing damage to optical components and coatings caused by high-power laser beams (Gogoll *et al.* 1996, Johansen *et al.* 1995a, Kelly *et al.* 1985). For such insulating materials, SEM inspection is often obscured by charging which makes it particularly difficult when damage features are minute and not evident from surface topography. Earlier SEM investigations of insulators concentrated either on a more global material characterization by varying the primary electron energy, E_p, (Böngeler *et al.* 1993, Kotera and Suga 1988, Postek *et al.* 1989, Vigouroux *et al.* 1986) or on local defect identification in laterally or vertically layered structures (Ishibashi *et al.* 1992, Kodama and Uchikawa 1992, Taylor 1981). However, we are not aware of systematic SEM studies of intrinsic or induced defect structures in which charging is either controlled or manipulated by varying E_p. In this contribution, we demonstrate the dramatic change of imaging information when altering E_p from low (< 1 keV) to high (20 keV) values. The aim was to achieve with both backscattered (BSE) and secondary (SE) electron detection high-contrast images of laser-generated microcracks and to gain a detailed understanding of large-scale charging with primary energy. To this purpose, we utilized an uncoated area of about 400 μm^2 at the surface of a solid CaF_2 crystal, which was localized near the rim of a laser-damaged spot and was therefore pervaded by microcracks.

Any analysis of electron-induced charging of electrically nonconducting areas inside a conducting (by coating) surrounding must pay attention to the lateral dimensions (Cazaux 1986, Johansen *et al.* 1996, Oh *et al.* 1993, Reimer *et al.* 1992). For a correct interpretation of the charge distribution inside such selected areas, it is important whether or not the surrounding is grounded or floating freely (Johansen *et al.* 1995b, Kotera and Suga 1988). Attempts to neutralize charging often result merely in a stabilization of the surface potential instead of a genuine charge compensation (Liehr *et al.* 1986). Such techniques include amplification or suppression of SE emission by applying a suitable potential between sample and detector (Postek *et al.* 1989), by heating the sample (Ogura *et al.* 1994), or by showering the surface with an additional defocused electron beam (Lambin *et al.* 1985, Liehr *et al.* 1986). Another point is that in SE imaging the apparent contrast does not necessarily reflect the surface charge. Backscattered electrons can simulate charging phenomena which are not actually present at the surface.

The surface potential is built up and stabilized by three mechanisms: (1) the deposition of primary electrons, (2) the yield and escape depth of SEs, and (3) the charge-induced increase of electrical conductivity in the irradiated region. The efficiency of these processes depends sensitively on the penetration depth of the primary electrons given by E_p. For each energy, an equilibrium is established between charge-up and leakage current. The conductivity is determined by material parameters such as mobility and lifetime of charge carriers,

This work was supported by the Deutsche Forschungsgemeinschaft, Sfb 337.

Address for reprints:
M. Reichling
Freie Universität Berlin
Fachbereich Physik
Arnimallee 14
14195 Berlin, Germany
E-mail: reichling@matth1.physik.fu-berlin.de

dielectric constant ε, and lateral extension of the conducting layer (Bommakanti and Sudarshan 1990, Liehr *et al.* 1986). The SE emission is governed by irradiation conditions such as primary electron energy and current density, scanning speed and area, as well as angle of incidence (Brunner and Schmid 1986, Ishibashi *et al.* 1992, Johansen 1994, Kotera and Suga 1988). The resulting depth variation of the charge distribution has the one-dimensional form (Ganachaud and Mokrani 1995, Kortov *et al.* 1979)

$$\rho(z) = \rho\left(1 - \frac{z}{z_1}\right)e^{-z/z_1} \tag{1}$$

where ρ_0 is the surface charge and z is the distance from the surface (positive for increasing depth). This charge distribution sets up an electric field

$$F(z) = \frac{\rho_0}{\varepsilon\varepsilon_0} z \cdot e^{-z/z_1} \tag{2}$$

inside the crystal. The field gradient toward the surface stimulates electron emission for $z < z_1$ (Fitting *et al.* 1978) while more negative charge is deposited in the crystal for $z > z_1$. The variation of these quantities with depth is illustrated in Figure 1. For the interpretation of SEM pictures, it is important to note that z_1 is a monotonic function of the incident electron energy.

Independent of the detection mode, there are two critical energies, E_1 and E_2, at which the crystal is neutral because the deposited charge is compensated by SE emission. At other energies, the charge density at the surface can be either positive for $E_1 < E_p < E_2$, or negative for $E_p < E_1$ and $E_p > E_2$. When the coefficients for SE emission, δ_{SE}, and for the backscattered fraction of primary electrons, η_{BSE}, obey the relation $\delta_{SE} < 1-\eta_{BSE}$, negative carriers dominate at the surface, while

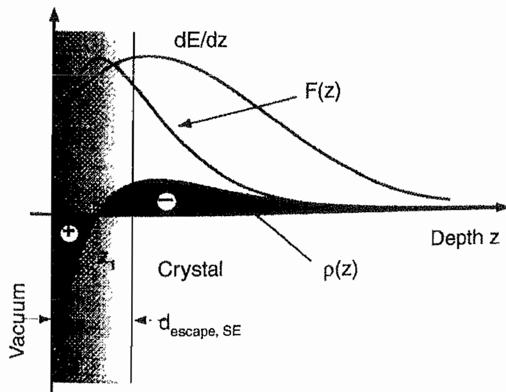

FIG. 1 Variation of primary electron energy loss, *dE/dz*, the resulting charge distribution $\rho(z)$ [Eq.(1)], and the electric field F(z) inside an electron irradiated insulator [Eq.(2)] (Kortov *et al.* 1979, Ganachaud and Mokrani 1995). SE = secondary electron.

for $\delta_{SE} > 1-\eta_{BSE}$ the surface charges positively (Cazaux 1986, Reimer *et al.* 1992). The latter is the case for a shallow penetration depth, that is, low energies of the primary electrons, allowing the SEs to escape. For higher energies, the primary electrons penetrate deeper and the SEs are stopped before reaching the surface and remain in the crystal. We determined the true surface potential E_s of the specimen area under study for the primary electron energies E_p used in contrast studies by means of an energy-dispersive spectrometry (EDS) detector to measure the Duane-Hunt high-energy cut-off E_{DH} of the Bremsstrahlung (Heinrich 1981); results are displayed in Table I. This provides accurate information about the landing energy of the primary electrons on the insulator surface over the interesting energy range, indicating that the difference $E_p - E_{DH}$ is relatively small compared with what is found for other highly insulating materials such as quartz or teflon that easily charge up to the primary energy.

Sample and Imaging Method

The object of our investigations was the trapezoidal bright area marked by T_c near the rim of the laser-damaged spot, shown in Figure 2. The history of this spot was as follows: The (111)-surface of a polished CaF_2 crystal ($20 \times 20 \times 6$ mm^3) was irradiated in air by a single laser pulse of 248 nm wavelength with 14 ns duration and top-hat profile. The fluence causing the heavy fracture seen in Figure 2 was 19.5 J/cm^2, well above the damage threshold (Gogoll *et al.* 1996). During the pulse, one of the fragments was hurled to the upper rim of the irradiated area. For the purpose of SEM imaging, the surface was then coated with a conducting 15 nm carbon layer. After the coating procedure, this fragment was blown off, leaving behind the uncoated trapezoidal-shaped area of about 400 μm^2 size. This area is of interest for two reasons: (1) It is located in a region with a high density of microcracks but no large-scale fragmentation. These microcracks can be utilized to define the image quality. They originate from thermoelastic tension caused by the strong lateral thermal gradient at the periphery of the laser irradiated spot (Johansen *et al.* 1995a, Gogoll *et al.* 1996). (2) The uncoated insulating area provides an ideal testing ground for charging phenomena in laterally limited dimensions surrounded by a well-defined (grounded) potential. Hence, we have to distinguish between the local contrast of the microcracks and the areal contrast of the whole uncoated area against the grounded surrounding.

Surface charging and image contrast of these microcracks have been investigated in the energy range 1 keV $< E_p <$ 20 keV with both BSEs and SEs. The carbon-coated part of the

TABLE I Compilation of Duane-Hunt cut-off energies E_{DH} obtained from a Bremsstrahlen analysis performed with an energy-dispersive spectrometry detector for a set of primary energies E_p.

E_p(keV)	1.2	1.5	2	5	10	12	15	20
E_{DH}(keV)	0.9	1.2	1.7	4.4	8.8	10.7	13.2	18.5

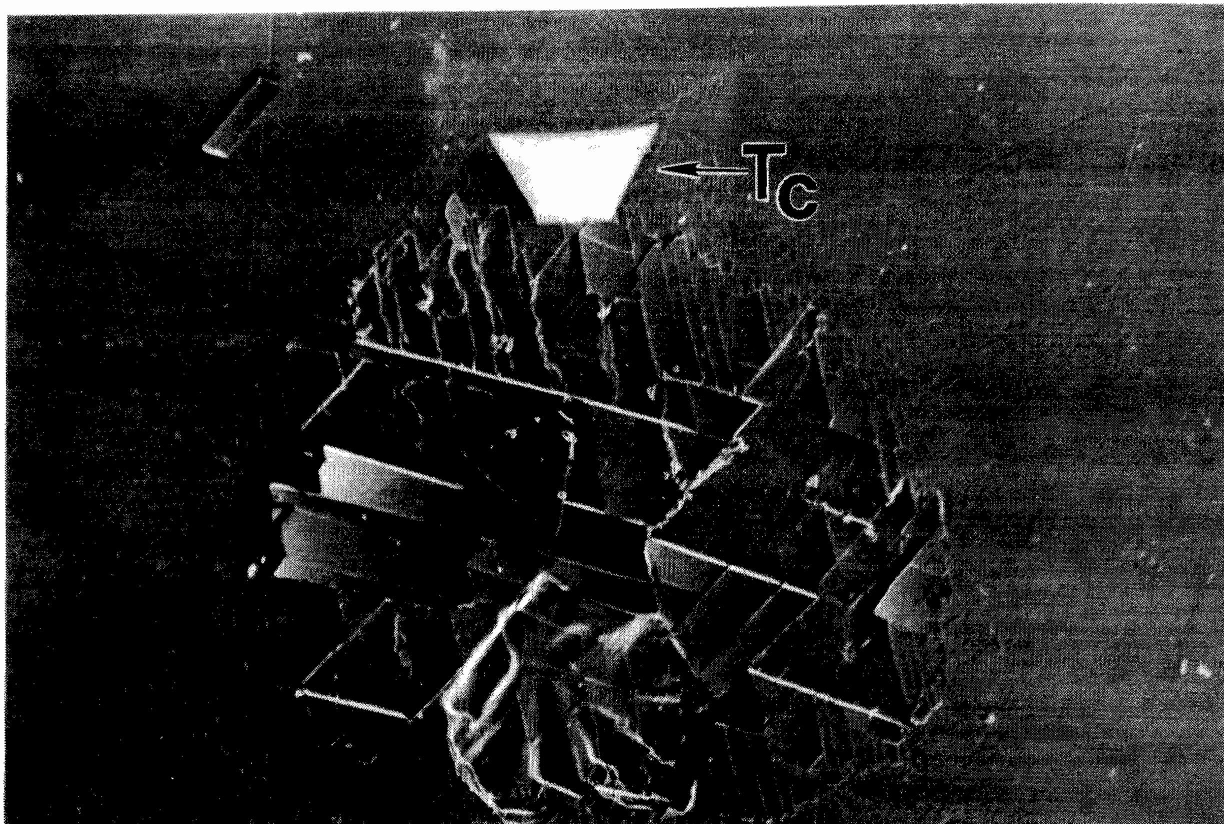

FIG. 2 Laser damage of polished CaF_2(111) generated by a single 14 ns pulse with 248 nm wavelength. The surface was coated with carbon except for the bright trapezoidal area at the upper rim, marked T_c, which served to study charging phenomena in laterally limited extensions. The image was recorded in secondary electron mode with $E_p = 2$ keV, and a surface inclination of $\phi = 25°$. Horizontal field width = 190 μm.

crystal surface was always grounded. The detection schemes are sketched in Figure 3. Backscattered electrons were detected at $\phi = 0°$ inclination in composition mode ($S_1 + S_2$), where S_1 and S_2 are the signals of the two semiconductor detectors D_1 and D_2, placed at a variable distance d from the surface (Fig. 3a). When the two detector signals are added, any topographic contrast is eliminated, while it is maximized when the two signals are subtracted. Imaging in SE mode was carried out at the two inclinations $\phi = 0°$ and 25°, as indicated in Figure 3b. By comparing the results for the two angles, backscattering effects of the primary electrons could be identified. In all SE measurements, the detector was biased at an accelerating potential of +300–600 V with regard to the grounded (coated) surface. Imaging was performed with nA currents in slow scan manner (40 ms/line) with a frame time of 80 s. Image contrasts were found to be independent of the primary electron current.

Results

Backscattered Electron Contrast

Backscattering of electrons is governed by the electric field distribution given in Eq. (2) and can therefore be utilized for

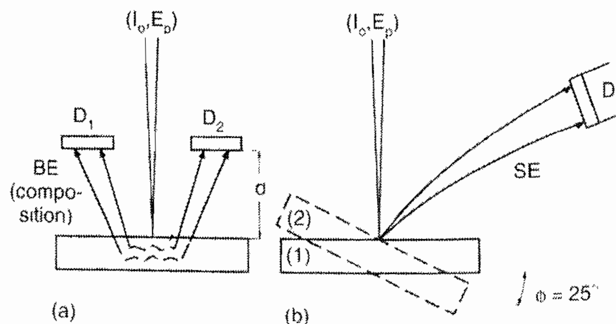

FIG. 3 Scanning electron microscopy detection schemes used in this contribution. (a) Backscattered electron composition and topography modes; (b) secondary electron detection with surface inclination of $\phi = 0$ and 25

studying the change of surface potential with primary electron energy. Employing composition contrast that is not sensitive to topography, we recorded a great number of images at perpendicular incidence ($\phi = 0°$). Selected examples for various primary energies are presented in Figure 4a–d. Generally, we observe stable charging conditions for $E_p > 6$ keV which allow us to obtain an undisturbed image of the fractured surface. In this range, elastically BSEs have sufficiently high energies not to be affected by surface charging. This is best

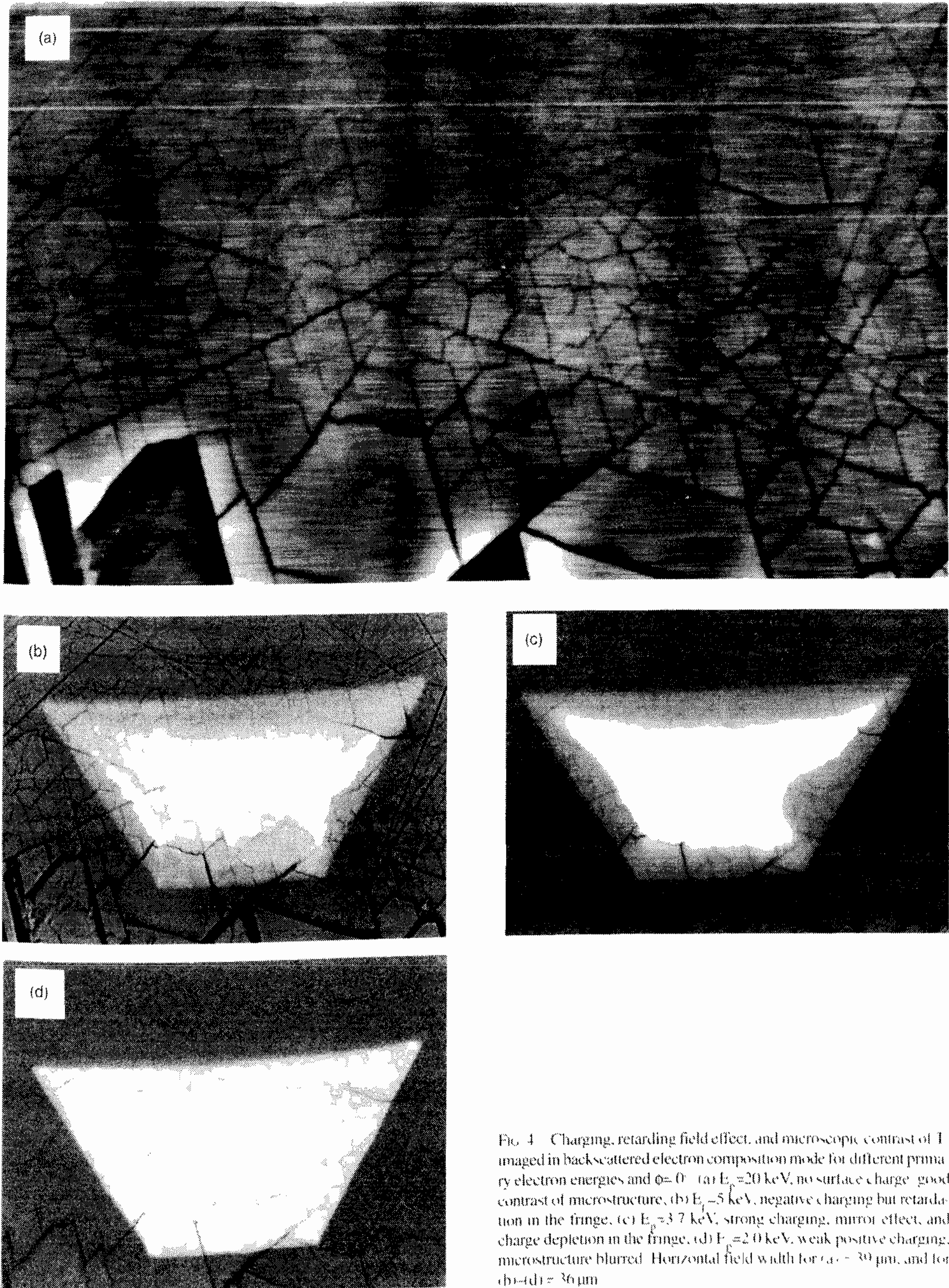

FIG. 4 Charging, retarding field effect, and microscopic contrast of I imaged in backscattered electron composition mode for different primary electron energies and $\phi = 0°$. (a) $E_p = 20$ keV, no surface charge, good contrast of microstructure, (b) $E_p = 5$ keV, negative charging but retardation in the fringe, (c) $E_p = 3.7$ keV, strong charging, mirror effect, and charge depletion in the fringe, (d) $E_p = 2.0$ keV, weak positive charging, microstructure blurred. Horizontal field width for (a) = 39 μm, and for (b)–(d) = 36 μm

demonstrated for $E_p = 20$ keV in Figure 4a, where the uncoated trapezoidal area T_c, identified in Figure 2, cannot even be distinguished from its surrounding. On the other hand, local variations of backscattering still provide a sharp image of microcracks which absorb electrons and appear as dark features; that is, the crack acts as a low-density region with an atomic number close to zero.

With decreasing E_p, the electrons penetrate less deeply into the crystal and are also more strongly repelled by the build-up of a negative surface charge. The BSE intensity increases and the trapezoid appears as a bright feature (Fig. 4b). For a certain primary energy, the negative charge-up can reach a degree where the surface layer acts like a mirror, as illustrated in Figure 4c. Here the potential is so strong that the working distance had to be increased from 8 to 18 mm to avoid image blinding. The other observation in Figure 4b and c is the retarding field effect, that is, the influence of the surrounding carbon layer at ground potential. Clearly, negative charge from the periphery of the uncoated area flows to the grounded layer, inhibiting the "mirror" effect in this boundary zone. For our scan speed (40 ms/line), the charge depletion range extends up to 2 µm and should generate an electric field up to 2×10^7 V/cm, which would by far exceed the breakdown threshold of the pure crystal. The fact that no breakdown occurs proves that there exists a high charge-induced conductivity near the surface.

For uncovered insulator surfaces of this insulator > 5 µm^2 and $E_p < 6$ keV, there is no chance to detect BSE images that are not affected by charging. The situation changes for $E_p \leq E_2$, where the negative surface charge vanishes and a positive one develops. This positive charging influences the BSE and the image loses both contrast and brilliance. A typical example is shown in Figure 4d and demonstrates that for primary electrons of $E_p = 2$ keV it becomes difficult to register sharp contours. The value for E_2 (ϕ=0°) given in the literature is 1.9 keV (Reimer *et al.* 1992).

The pictures in Figure 4a–d were taken in additive composition mode which eliminates any topographic contrast. In order to check that there are indeed no topographic features present inside T_c, the same area was scanned in topographic mode, (S_1–S_2), with 20 keV primary electron energy as used for Figure 4a. The result is displayed in Figure 5. Comparison with Figure 4a reveals that within the trapezoidal area there are no bent-up edges and the surface, although penetrated by microcracks, is perfectly flat. At the boundary toward higher laser damage, however, the topographic contrast shows edge contours of missing fragments. Again, the high primary electron energy of 20 keV rules out any influence of charging.

Secondary Electron Contrast

Secondary electrons originate in the near surface range and are expected to be still more sensitive to surface charging compared with BSE detection. It is therefore of interest to study also the SE image appearance as a function of primary

FIG. 5 Backscattered electron image in topography mode for $E_p = 20$ keV at perpendicular incidence. The trapezoidal area shows no topographic contrast. Features in the lower part of the picture represent missing or bent-up fragments outside T_c. Horizontal field width = 39 µm.

electron energy. The SE emission yield depends on the angle of incidence, ϕ, defined in Figure 3. The SE coefficient varies like $\delta_{SE} \propto \cos^{-1}\phi$ and is strongest at glancing incidence (Ishibashi *et al.* 1992). The primary energy component along the normal is $E_n = E_p\cos^2\phi$. Accordingly, the critical energy E_2 varies with ϕ, and the values given by Reimer *et al.* (1992) for CaF_2 are $1.9\ \text{keV} \leq E_2 \leq 3.0\ \text{keV}$ for $0° \leq f \leq 70°$. This variation can be utilized to obtain topographic information and to discern artefacts from BSEs. When interpreting SE images, the SE coefficients δ_{SE} of the covered and uncovered areas must be compared. According to the literature (Dekker 1958, Kanaya and Kawakatsu 1972) the SE yield of carbon varies between 0.90 (δ_{max}) and 0.36 over the energy range 0.3 to 3 keV, supporting the observed contrast variation as discussed in connection with Figure 7. For CaF_2, bulk data are not available; however, a maximum of $\delta_{SE}^{max} = 3.2$ has been given for a CaF_2 layer for an unspecified primary energy (CRC 1993). One should keep in mind, however, that laser irradiation causing microcracks also might have modified these material properties. For example, structural defects such as cracks and dislocations give rise to local deviations from the bulk band structure in form of electronic states in the band gap, which are expected to enhance the SE yield.

Figure 6a–d displays SE images recorded at $\phi=0°$ at energies ranging from 1.5 to 20 keV. From other images (not shown here), we know that maximal negative surface charging on T_c occurs around 15 keV in good agreement with the measured highest deviation of the Duane-Hunt high energy cut-off of the Bremsstrahlung of 1.8 keV for this primary electron energy (Table I). This can still be recognized for a primary energy of 12 keV shown in Figure 6b, where the bright appearance of the trapezoidal area signals negative charge-up. The reason is that the average penetration depth of the primary electrons is of the same order of magnitude as the mean free path of the SEs. The penetration depth for 12 keV electrons is about 1 μm (Fitting 1974), while precise data for the spectrum of SEs are not available. For a typical SE energy of 4.5 eV, however, an attenuation length of 260 nm in CaF_2 has been measured and transmission through a layer of 800 nm thickness was demonstrated (Quiniou *et al.* 1992). Hence, the charge loss in the surface layer due to emitted SEs is overcompensated by those that originate more inside the crystal

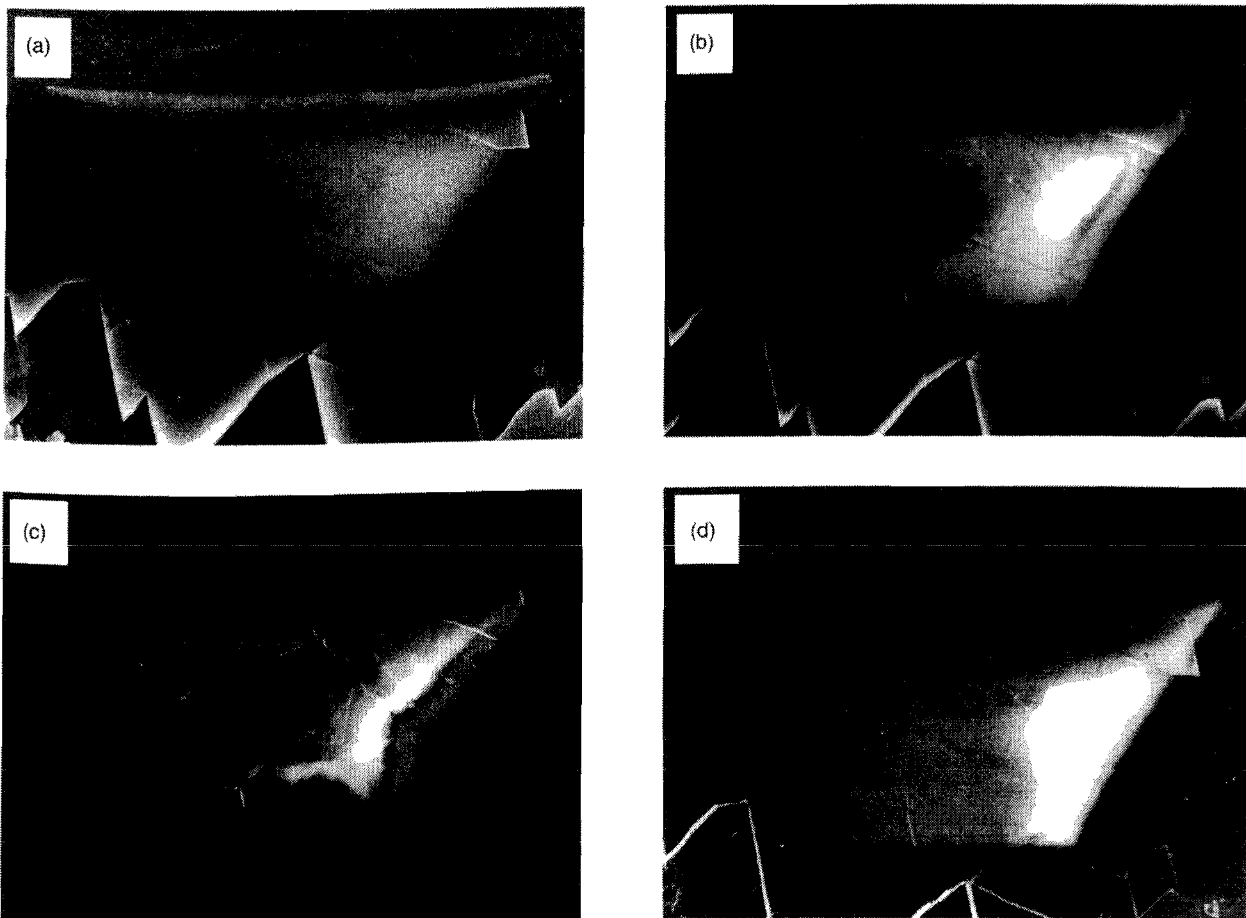

FIG. 6 Secondary electron imaging of T_c for different primary electron energies at $\phi=0°$. (a) E_p=20 keV, positive surface charge, microstructure blurred; (b) E_p=12 keV, strong negative charging, retardation in the fringe; (c) E_p=3.0 keV, weak negative charging, charge depletion in the fringe; (d) E_p=1.5 keV, weak positive charging, microstructure blurred. Horizontal field width = 36 μm.

and are stopped before leaving the surface. In contrast, for significantly higher primary electron energies, the negative charge distribution is located deeper inside the crystal and most of the SEs generated in that range never come close to the surface. Consequently, charge loss due to SE emission is not compensated and the surface charges positive, as can be recognized in Figure 6a. The trapezoidal area in Figure 6c is still somewhat negative since $E_p > E_2$, and a significant fraction of SE from deeper parts cannot escape the crystal. Finally, in Figure 6d, $E_p < E_2$ and we observe a darker image due to stronger SE emission and positive charging. The areal contrast in Figures 6a and d is quite similar despite the different physical origin.

From Figures 6a through d it becomes clear that SE detection at ϕ=0 is not very suitable for imaging microcracks. For slightly positively charged surfaces (Figs. 6a, d), SEs leaving the surface are retarded and bent, thereby blurring the contrast of the microcracks. In Figures 6b and c, the fracture pattern is discernible but by far not as distinct as in BSE contrast with high-energy primary electrons (cf. Fig. 4a).

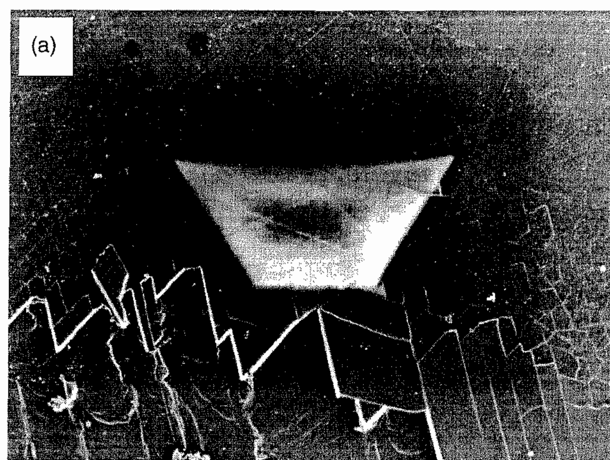

FIG. 7 Contrast inversion in secondary electron imaging at ϕ= 0° and low primary energies in the range $E_1 < E_p < E_2$, to illustrate a variation of δ_{SE} for carbon in this energy range. (a) E_p=1.5 keV, microcracks and polishing scratches clearly visible, (b) E_p=0.5 keV, visibility of all surface details strongly reduced. Horizontal field width = 64 μm.

Identification of negative or positive charging by brighter or darker contrast with respect to the grounded surroundings indicates that δ_{SE} of the carbon coating is dependent on E_p (Kanaya and Kawakatsu 1972) and cannot serve as a reference. Reimer and Tollkamp (1980) report on a δ_{SE} above 1.5 for energies of about 1 keV for light elements (3 ≤ atomic number ≤ 13). Therefore, we expect a strong dependence of the contrast from E_p for low primary energies. This can be seen in Figure 7a and b. Both SE images are recorded at $\phi = 0°$ with low primary energies in the range $E_1 < E_p < E_2$, which implies that in both cases the trapezoidal area is positively charged. Obviously, its appearance in both pictures is dramatically different with reference to the brightness of the surrounding carbon coating. Assuming instead that the trapezoidal area should be of comparable brightness at both energies, then the graphite coating would have a drastically different appearance in both pictures, implying that δ_{SE} would change. To avoid such ambiguities, it is advisable to define a relative image contrast K of the form

$$K = |I_c - I_u| / (I_c + I_u) \tag{3}$$

where I_c and I_u are the SE intensities from coated and uncoated areas, respectively. Another important observation is that in Figure 7a and b the information about microcracks is lost, perhaps more completely in Figure 7b. This would indicate a stronger positive charging at E_p = 0.5 keV. Furthermore, it is interesting to note in Figure 7b that compared with Figure 7a, also in the vicinity of T_c, fracture features cannot be recognized anymore. For a primary energy of 0.5 keV, the range of electrons in carbon is about 15 nm (Fitting 1974) and corresponds to the thickness of the carbon layer. Under these imaging conditions, the maximum depth of information of the SEs cannot be larger than the depth of the carbon layer and, therefore, the SE image does not reflect features from the surface of the CaF_2 crystal. Notice also that the imaging conditions were identical in Figures 6d and 7a.

Figure 8 displays SE images recorded with different primary energies at a tilt angle of ϕ = 25°. Again the detector was at an accelerating bias of several hundred volts. The inclination reduces the areal contrast by $\cos^2\phi$ = 0.82 but enhances the topographic contrast outside the trapezoidal area. According to Reimer *et al.* (1992), the critical energy is now E_2 = 2.3 keV. Again, the areal contrast of T_c varies strongly from E_p. However, charging is compensated in part by the $\cos^{-1}\phi$-dependence of SE emission on ϕ. In Figure 8a, the effective energy is 16.4 keV and the surface carries a negative charge. Microcracks are clearly visible but appear bright, indicating an enhanced SE emission. The brilliance of T_c is amplified by primary electrons scattered into the detector. The negative charging becomes much weaker in Figure 8b, with the effective (corrected for ϕ) primary energy approaching E_2. The microcracks can still be seen as bright lines, but are not as sharp as observed with higher energy in Figure 8a. In Figure 8c, the trapezoidal area is positively charged but, because of

FIG. 8 Secondary electron imaging of T_c for different primary electron energies at ϕ=25°. (a) E_p=20 keV, negative charging, fringe retardation, sharp microstructure; (b): E_p=5 keV, weak negative charging, fringe retardation, microstructure visible; (c): E_p=2.0 keV, weak positive charging, faint microstructure; (d): E_p=1.0 keV, strong positive charging, faint microstructure. Horizontal field width for (a), (c), (d), = 36 μm and for (b) = 39 μm.

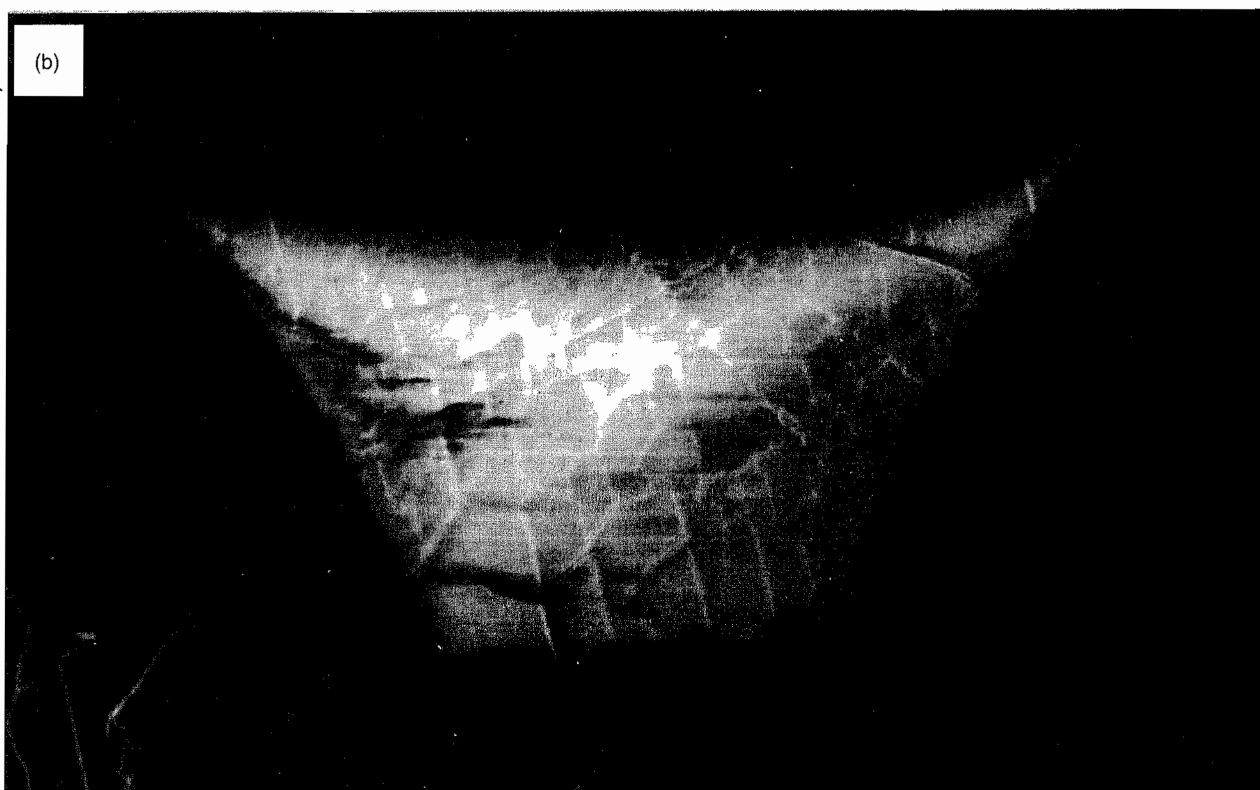

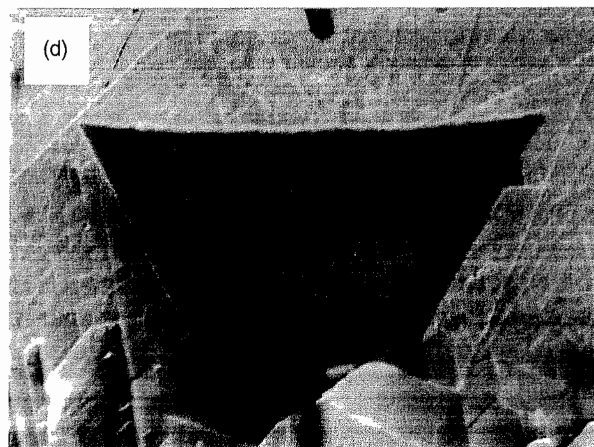

the ratio $\delta_{SE}(CaF_2)/\delta_{SE}(C) \approx 3.2$, it still appears brighter than the carbon surrounding. The positive charge-up is still stronger in Figure 8d, but a major fraction of SEs is bent or retracted to the surface. Consequently, the trapezoidal area turns darker despite the fact that more SEs are expected to leave the surface at such low primary energy.

Concerning local information, microcracks are barely visible in Figure 8c and d and appear, if at all, as faint dark lines. This points toward reduced SE emission out of cracks at low primary energies, possibly because they are held back by the positive charge-up. The opposite happens for $E_p > E_2$, where microcracks appear as bright lines in Figure 8a and b, implying stronger SE emission from fractured areas. Geometrical edge effects can be ruled out by the even appearance of the microcracks. Also, the topographic contrast in Figure 5 shows that the surface of the trapezoidal area is perfectly flat without upcast edges. To interpret the bright lines, we note that the tilt of the sample opens the path for electrons from inside the cracks toward the detector, and we suggest that δ_{SE} is enhanced at or near the walls of microcracks. The reason is sought in more weakly bound occupied states within the band gap of insulators (Bommakanti and Sudarshan 1990). Such electronic states are expected for structural defects such as fractured planes, steps, and dislocations. Although the bright pattern of microcracks can be well recognized in Figure 8a and b, SE imaging at $\phi = 25°$ does not provide by far such distinct fracture contrast as that obtained in BSE composition mode with high primary energies (compare Fig. 4a).

Discussion

As stated before, the charge contrast of the trapezoidal area T_c in Figure 2 with respect to the surrounding grounded carbon-coated surface is the result of a delicate balance between the depth distribution of the deposited charge, the depletion by the re-emitted charge, and the electrical conductivity of the inspected area. Despite the fact that CaF_2 is one of the best ionic conductors ($\gamma^{-1} \approx 10^{13}$ Ωcm, according to Sullivan *et al.* 1982), with a bulk charge relaxation time of $\tau = \varepsilon\varepsilon_0/\gamma \approx 7$s, a stabilization of the surface potential can only be reached for a laterally limited area inside a conducting surrounding at ground potential (size effect). In addition to the properties of the pure crystal, the observed degree of charging may also be influenced by laser-induced crystal modifications like, for example, thermally generated dislocations which can act as electron traps (Webb *et al.* 1993). Further investigations are required to elucidate this question.

In SE mode with perpendicular incidence (ϕ=0°), it is difficult to find charge-free conditions for the trapezoidal area. At primary energies 2.5 keV $\leq E_p \leq$ 15 keV, we observe different degrees of negative charging in form of varying brightness. The turning point into positive surface charging for $E_p \geq$ 15 keV is characterized by total blurring of the fracture pattern. Then the deposited negative charge penetrates too deeply into the bulk to neutralize the charge loss by SE emission. For small primary energies ($E_p \leq$ 2.5 keV), on the other hand, the SE emission dominates strongly and causes a similar positive charge-up. Again, the microcracks are no longer discernible.

The degree of charging can be reduced by tilting the sample, which in effect reduces the primary energy. The contrast of the microcracks can actually be used as a measure for the charge reduction. For a tilt angle of ϕ=25°, the distortion due to surface charging can be minimized in the energy range 4 keV $\leq E_p \leq$ 6 keV. At these energies, we also observe a stronger SE emission from the microcracks which makes them appear bright. Undoubtedly, this effect carries information about the electronic structure at the crack boundaries, but the dependence of δ_{SE} on the binding energy of electronic defect states needs further investigation.

Negative surface charging in SE and BSE imaging is to a certain extent complementary since in SE mode at ϕ=25°, scattering of primary electrons into the detector vanishes with decreasing E_p at about the same energy where negative charge-up appears in BSE additive composite mode. From Figures 4 and 8 and many other images not shown here we find this value to be about $E_p \approx$ 6 keV, which is equivalent to an electron penetration depth R_e of about 0.4 µm. This value corresponds to the depth range of polishing damage for these crystals, which was determined to be about 0.3 µm (Dietrich *et al.* 1977, Gogoll *et al.* 1996). Within this depth, the density of dislocations is much higher compared with the bulk crystal which causes among others an increase of optical absorption. It is conceivable that this "mosaic-structured" range causes an increased backscattering of primary electrons. This conjecture is supported by the sharp maximum of "mirror-like" negative charging at 3.7 keV, displayed in Figure 4c, which is generated by strong backscattering out of a shallow region of about 0.5 R_e thickness (Shimizu and Murata 1971, Werner and Johansen 1987). For $E_p >$ 5 keV (Fig. 4b), the penetration depth exceeds the layer thickness damaged by polishing, and negative charging by backscattering ceases quickly with increasing primary energy. A systematic investigation of the variation of negative charging with primary energy might actually provide further insight into the problem of damage depth caused by polishing.

Conclusions

In this contribution we systematically explored the potential of SEM for investigating microdamage of insulator surfaces. In view of charging, the aim was to find optimal imaging conditions for obtaining information about laser-induced microcracks in BSE or SE modes. An uncoated spot at the periphery of a laser-damaged area served to investigate both the lateral extension of charging (size effect) and the local contrast of microcracks. The contrast variation with primary electron energy was studied and threshold values for the onset of negative or positive charging were determined for BSE and SE imaging. Backscattered electrons were detected in additive (composition) and subtractive (topography) modes. Secondary electrons were measured at 0° and 25° surface inclination. A given charge state defined by the primary elec-

tron energy appeared to be quite different in these different detection modes. In addition, in SE imaging, tilted samples could scatter high-energy primary electrons into the detector. This would introduce artificial brightness in the micrograph and outshine structures due to the actual charge state of the surface.

The most distinct local contrast of microcracks is obtained in BSE composition mode with 20 keV primary electrons. With decreasing energies the cracks are blurred first by negative charge-up ("mirror effect") and at still lower energies by positive charging. Secondary electrons, on the other hand, are not very suitable for recording sharp images of microcracks. Because of their low energy, they are extremely sensitive to positive surface potentials. Only for tilted samples and energies around and above 5 keV do the microcracks appear as bright features with increased SE emission. This may be typical for electronic defect states with lower binding energy. Finally, the variation of electron penetration depth with primary energy points a way to explore subsurface defect distributions.

References

Bommakanti RG, Sudarshan TS: Influence of mechanical grinding and polishing operations of brittle polycrystalline alumina on the pulsed surface flashover performance. *J Appl Phys* 67, 6991–6997 (1990)

Böngeler R, Golla U, Kässens M, Reimer L, Schindler B, Senkel R, Spranck M: Electron-specimen interactions in low-voltage scanning electron microscopy. *Scanning* 15, 1–18 (1993)

Brunner M, Schmid R: Charging effects in low-voltage scanning electron microscope metrology. *Scan Electron Microsc* II, 377–382 (1986)

Cazaux J: Some considerations on the electric field induced in insulators by electron bombardment. *J Appl Phys* 59, 1418–1430 (1986)

CRC Handbook of Chemistry and Physics, 74th Edition, 1993–1994 CRC Press, Boca Raton, Ann Arbor, London (1993)

Dekker AJ: Secondary electron emission. *Solid State Phys* 6, 251–311 (1958)

Dietrich B, Förster E, Böttger R: Messung von Rockingkurven eines polierten CaF_2-Kristalls. *Kristall Technik* 12, 609–615 (1977)

Fitting H-J: Transmission, energy distribution and SE excitation of fast electrons in thin solid films. *Phys Stat Sol (a)* 26, 525–535 (1974)

Fitting H-J, Glaefeke H, Wild W: Energie- und Winkelanalyse von Exoelektronen. *Exper Tech Phys* 26, 253–259 (1978)

Ganachaud JP, Mokrani A: Theoretical study of the secondary electron emission of insulating targets. *Surf Sci* 334, 329–341 (1995)

Gogoll S, Stenzel E, Reichling M, Johansen H, Matthias E: Laser damage of CaF_2(111) surfaces at 248 nm. *Appl Surf Sci.* 96–98, 332–340 (1996)

Heinrich KFJ: *Electron Beam X-Ray Microanalysis.* Ch. 6, Van Nostrand Reinhold Company (1981) 154–186

Ishibashi Y, Kodama T, Oiwa H, Uchikawa Y: Analysis of electron range versus energy relationship of insulators in low-voltage scanning electron microscopy. *Scanning* 14, 219–223 (1992)

Johansen H: REM-Oberflächenabbildung eines massiven Dielektrikums vor und nach einer Excimerlaserbestrahlung. *Beitr Elektronenmikrosk Direktabb Oberfl* 27, 117–124 (1994)

Johansen H, Gogoll S, Stenzel E, Reichling M, Matthias E: SEM-analysis of fracture features formed in excimer-laser induced surface damage of CaF_2. *Radiation Effects and Defects in Solids* 136, 151–156 (1995a)

Johansen H, Gogoll S, Stenzel E, Reichling M: Scanning electron microscopical inspection of uncoated CaF_2 single crystals. *Phys Stat Sol (a)* 150, 613–624 (1995b)

Johansen H, Gogoll S, Stenzel E, Reichling M, Matthias E: Charging phenomena in low voltage electron microscopy of laser-fractured fluoride surfaces. *J Appl Phys* 80, 4928–4933 (1996)

Kanaya K, Kawakatsu H: Secondary electron emission due to primary and backscattered electrons. *J Phys D* 5, 1727–1742 (1972)

Kelly R, Cuomo JJ, Leary PA, Rothenberg JE, Braren BE, Aliotta CF: Laser sputtering Part I: On the existence of rapid laser sputtering at 193 nm. *Nucl Instr Meth Phys Res* B9, 329–340 (1985)

Kodama T, Uchikawa Y: Conditions of energy and incident angle of primary beam for observation of insulators' surface by SEM. *J Electron Microsc* 41, 65–69 (1992)

Kortov V, Isakov V, Gaprindoshvily A, Fitting H-J, Glaefeke H, Wild W: Untersuchung des Austritts von Exoelektronen aus geladenen Isolatorschichten mit Hilfe des Monte-Carlo-Verfahrens. *Phys Stat Sol (a)* 54, 633–638 (1979)

Kotera M, Suga H: A simulation of keV electron scattering in a charged-up specimen. *J Appl Phys* 63, 261–268 (1988)

Lambin P, Vigneron J P, Lucas A A: Electron-energy-loss spectroscopy of multilayered materials: Theoretical aspects and study of interface optical phonons in semiconductor superlattices. *Phys Rev* B 32, 8203–8215 (1985)

Liehr M, Thiry PA, Pireaux JJ, Caudano R: Characterization of insulators by high-resolution electron-energy-loss spectroscopy: Application of a surface-potential stabilization technique. *Phys Rev* B 33, 5682–5697 (1986)

Ogura K, Suzuki T, Sato T, Sueyoshi T, Ikegami T, Hertsens RC: Observation of non-conductive specimens using "specimen heated and electron beam induced conductivity (SHEBIC)" method with an ultrahigh-resolution SEM. *Proc 13th Int Congr Electr Micr* Vol.1, 129–130 (1994)

Oh KH, Ong CK, Tan BTG, Le Gressus C, Blaise G: Variation of trapping/detrapping properties as a function of the insulator size. *J Appl Phys* 74, 1960–1967 (1993)

Postek MT, Keery WJ, Larrabee RD: Specimen biasing to enhance or suppress secondary electron emission from charging specimens at low accelerating voltages. *Scanning* 11, 111–121 (1989)

Quiniou B, Schwarz W, Wu Z, Osgood RM, Yang Q: Photoemission from thick overlying epitaxial layers of CaF_2 on Si(111). *Appl Phys Lett* 60, 183–185 (1992)

Reimer L, Golla U, Böngeler R, Kässens M, Schindler B, Senkel R: Charging of bulk specimens, insulating layers and free-supporting films in scanning electron microscopy. *Optik* 92, 14–22 (1992)

Reimer L, Tollkamp C: Measuring the backscattering coefficient and secondary electron yield inside a scanning electron microscope. *Scanning* 3, 35–39 (1980)

Shimizu R, Murata K: Monte-Carlo calculations of the electron sample interactions in the scanning electron microscope. *J Appl Phys* 42, 387–394 (1971)

Sullivan PW, Farrow RFC, Jones GR: Insulating epitaxial films of BaF_2, CaF_2 and $Ba_xCa_{1-x}F_2$ grown by MBE in InP substrates. *J Crystal Growth* 60, 403–413 (1982)

Taylor DM: Electron-beam-induced conductivity and related processes in insulating films. *IEE Proc* 128, Pt. A, 174–182 (1981)

Vigouroux JP, Duraud JP, Le Moel A, Le Gressus C: Electron trapping in amorphous SiO_2 studied by charge buildup under electron bombardment. *J Appl Phys* 57, 5139–5144 (1986)

Webb RL, Jensen LC, Langford SC, Dickinson JT: Interactions of wide band-gap single crystals with 248 nm excimer laser radiation. I. MgO. *J Appl Phys* 74, 2323–2337 (1993)

Werner U, Johansen H: Scanning electron microscopy: Physical foundations of contrast formation. Ch.7. In *Electron Microscopy in Solid State Physics* (Eds. Bethge H, Heydenreich J). Elsevier Science Publishing Co., Amsterdam (1987) 170–201